

# Natural Quasicrystals

Luca Bindi,<sup>1</sup> Paul J. Steinhardt,<sup>2\*</sup> Nan Yao,<sup>3</sup> Peter J. Lu<sup>4</sup>

Quasicrystals are solids whose atomic arrangements have symmetries that are forbidden for periodic crystals, including configurations with fivefold symmetry. All examples identified to date have been synthesized in the laboratory under controlled conditions. Here we present evidence of a naturally occurring icosahedral quasicrystal that includes six distinct fivefold symmetry axes. The mineral, an alloy of aluminum, copper, and iron, occurs as micrometer-sized grains associated with crystalline khatyrkite and cupalite in samples reported to have come from the Koryak Mountains in Russia. The results suggest that quasicrystals can form and remain stable under geologic conditions, although there remain open questions as to how this mineral formed naturally.

Solids, including naturally forming minerals, are classified according to the order and rotational symmetry of their atomic arrangements. Glasses and amorphous solids have disordered arrangements with no exact rotational symmetry. Crystals have atomic structures with long-range periodic order that can be described by a single atom or atomic cluster that repeats at regular intervals. According to the well-known theorems of crystallography derived nearly two centuries ago, the rotational symmetries of crystals are highly restricted: Two-, three-, four-, and sixfold symmetry axes are allowed, but five-, seven-, and all higher-fold symmetry axes are forbidden. Quasicrystals (1, 2) (short for quasiperiodic crystals) have a more subtle kind of long-range order. In a quasiperiodic structure, the atomic positions along each symmetry axis are described by a sum of two or more periodic functions whose wavelengths have an irrational ratio (inexpressible as a ratio of integers). This difference exempts quasicrystals from the crystallographic restrictions: They can exhibit all the rotational symmetries forbidden to crystals, including fivefold symmetry. Just as square or hexagonal tilings are commonly used as geometric analogs for periodic crystals, the Penrose tiling (3) is used as an analog for quasicrystals. The fivefold symmetric tiling consists of acute and obtuse rhombic tiles that repeat along each symmetry direction with frequencies whose quotient is  $\tau = \frac{1+\sqrt{5}}{2} = 1.618$ , the golden ratio.

The concept of quasicrystals was introduced 25 years ago (1), and the first example observed was a rapidly quenched alloy of Al and Mn with icosahedral symmetry (2). Since then, over 100 examples have been identified (4), but all have been synthetic alloys produced in the laboratory under controlled conditions, ranging from fast to moderately slow quenching (5). A substantial

number have icosahedral symmetry, but other crystallographically forbidden symmetries have been observed as well (1, 4). Among the most carefully studied is the icosahedral phase of AlCuFe (i-AlCuFe), reported by Tsai *et al.* (6) and subsequently examined over a range of stoichiometries, temperatures, and quench conditions (5). The optimal composition,  $\text{Al}_{63}\text{Cu}_{24}\text{Fe}_{13}$ , is known to be stable over the temperature range from 500° to 870°C at atmospheric pressure, but its stability under wider ranges of temperature and pressure has not been fully explored.

To search for quasicrystals beyond the chemical families in which they are already known to occur, a scheme to identify quasicrystals based on powder diffraction data was developed and applied (7) to a collection of over 80,000 patterns published as the “powder diffraction file” by the International Center for Diffraction Data (ICDD-PDF). The ICDD-PDF includes some 9000 mineral patterns in addition to synthetic phases. Figures of merit were identified to rank the observed powder patterns according to how they compared with those of ideal quasicrystals. Known quasicrystals in the ICDD-PDF were successfully identified by this procedure. Among other materials, samples of the 50 most highly ranked were obtained and explored with transmission electron microscopy (TEM) and powder x-ray diffraction (XRD), but no new quasicrystals, synthetic or natural, were found (7). As a result, the search turned to possibilities outside the existing catalog, beginning with minerals with compositions similar to those of known quasicrystals synthesized in the laboratory.

Many synthetic quasicrystals are metallic alloys, often including Al, which led to the consideration of the mineral khatyrkite, with a nominal composition of  $(\text{Cu,Zn})\text{Al}_2$ . Khatyrkite (8, 9) was originally found in a metal placer, reported as coming from a Triassic (200 million years old) ultramafic (silicon-poor) zone (10) of the Koryak Mountains, northeast of the Kamchatka Peninsula in Russia. Cupalite, nominally  $(\text{Cu,Zn})\text{Al}$ , is reported to form in close association with khatyrkite and is orthorhombic (8, 9). The only reported samples of khatyrkite were described as roughly 30- $\mu\text{m}$  grains found in association with weathered serpentinite and located near the Listvenitovy Stream in the Chetkinvaia metamorphic melange (9, 10).

We examined a khatyrkite-bearing sample from the collection of the Museo di Storia Naturale of the Università degli Studi di Firenze (catalog number 46407/G) that was acquired in 1990 and cataloged as coming from the Koryak region, although we have no direct evidence that our sample originated from the same location as the type specimen. Instead of a metal placer, the sample includes an assemblage (Fig. 1A) of spinel, augite, and forsteritic olivine. We made polished thin sections and examined the microstructure using backscattered electron (BSE) imaging in the scanning electron microscope (11). To quantify the stoichiometry of these phases, we examined samples using wavelength-dispersive x-ray analysis in an electron microprobe (12).

The study revealed a number of Al-rich grains consistent with khatyrkite and cupalite, though with only traces of Zn as compared with the reported composition (8, 9). These grains were intergrown with forsteritic olivine (Fig. 2A) and an unknown mineral, AlCuFe, corresponding to the  $\beta$  phase (5) in the synthetic Al-Cu-Fe alloy (Fig. 2B). The complex assemblage of mineral phases shown in Figs. 1 and 2 provides evidence

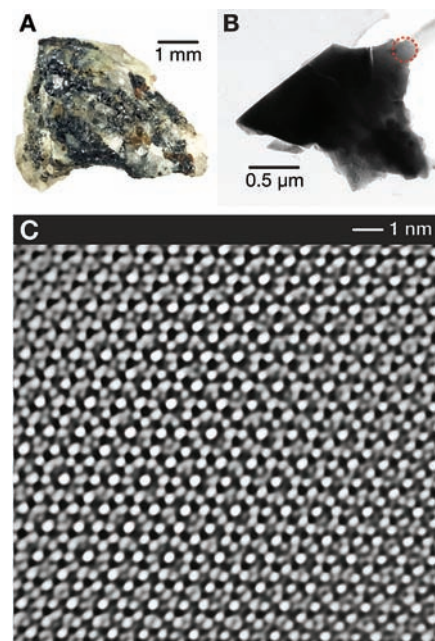


**Fig. 1.** (A) The original khatyrkite-bearing sample used in the study. The lighter-colored material on the exterior contains a mixture of spinel, augite, and olivine. The dark material consists predominantly of khatyrkite and cupalite (CuAl) but also includes granules, like the one in (B), with composition  $\text{Al}_{63}\text{Cu}_{24}\text{Fe}_{13}$ . The diffraction patterns in Fig. 4 were obtained from the thin region of this granule indicated by the red dashed circle, an area 0.1  $\mu\text{m}$  across. (C) The inverted Fourier transform of the HRTEM image taken from a subregion about 15 nm across displays a homogeneous, quasiperiodically ordered, fivefold symmetric, real space pattern characteristic of quasicrystals.

<sup>1</sup>Museo di Storia Naturale, Sezione di Mineralogia, Università degli Studi di Firenze, Firenze I-50121, Italy.

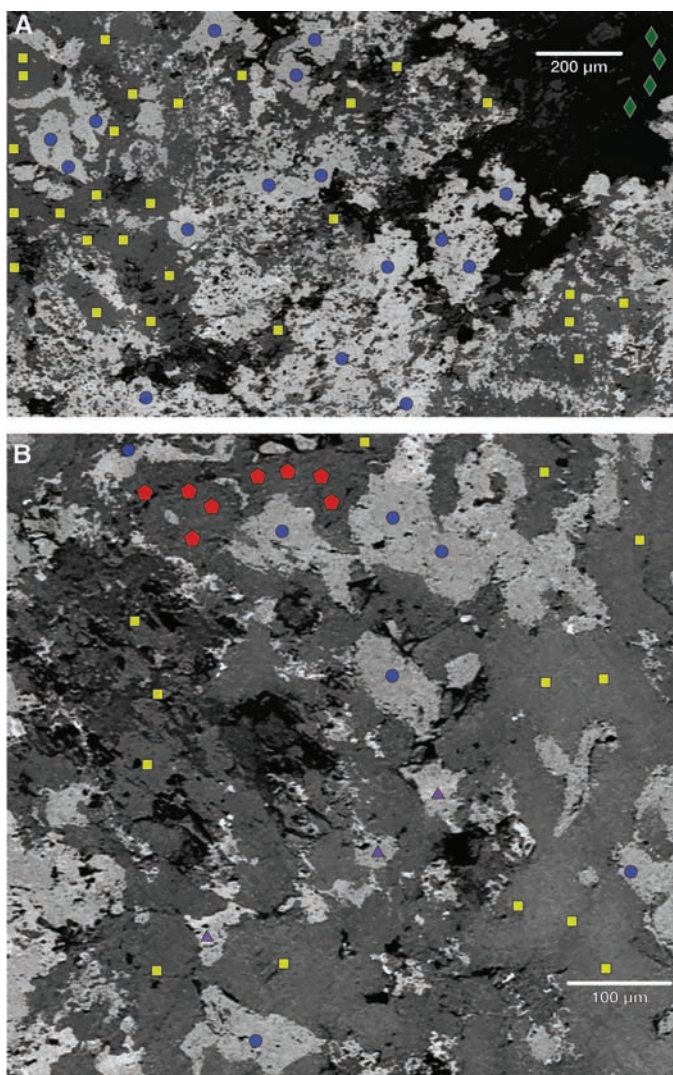
<sup>2</sup>Princeton Center for Theoretical Science, and Joseph Henry Laboratories, Department of Physics, Princeton University, Princeton, NJ 08544, USA. <sup>3</sup>Princeton Institute for the Science and Technology of Materials, Princeton University, Princeton, NJ 08544, USA. <sup>4</sup>Department of Physics and School of Engineering and Applied Sciences, Harvard University, Cambridge, MA 02138, USA.

\*To whom correspondence should be addressed. E-mail: steinh@princeton.edu

**Table 1.** Best fit of the powder XRD pattern from the mineral sample to an ideal FCI quasicrystal, using the automated scheme in (7). The first two columns show the magnitude of the scattering vector  $|\mathbf{Q}|$  for the real and ideal patterns, and column three shows the difference between these two values. The fourth column is the relative intensity (100 is the most intense). The fifth column is the best-fit index assignment (integer linear combinations of the six vectors  $\{\mathbf{g}_k, \mathbf{g}_5\}$ ), and the last column is an equivalent two-integer index introduced by Janot (4) (eqs. 3.20 to 3.26) and used in Fig. 3A, in which  $\mathbf{Q} = \frac{\sqrt{N+\tau M}}{d}$  with distance  $d = 34 \text{ \AA}$  and six-dimensional lattice parameter  $a_6 \equiv \frac{d}{\sqrt{2(2+\tau)}} = 12.64 \text{ \AA}$ .

$ \mathbf{Q}_{\text{real}}  (\text{\AA}^{-1})$	$ \mathbf{Q}_{\text{ideal}}  (\text{\AA}^{-1})$	$\Delta$	$I_{\text{rel}}$	$n_i$	$(N, M)$
0.1116	0.1120	0.32%	2	200000	(8,4)
0.1808	0.1812	0.20%	5	111111	(12,16)
0.2668	0.2670	0.06%	20	200022	(24,36)
0.2931	0.2932	0.03%	25	311111	(28,44)
0.3082	0.3083	0.03%	20	220022	(32,48)
0.3571	0.3576	0.12%	5	311131	(44,64)
0.4080	0.4078	0.05%	10	420022	(56,84)
0.4255	0.4254	0.02%	5	311133	(60,92)
0.4744	0.4744	0.00%	90	422222	(72,116)
0.4985	0.4988	0.06%	100	402042	(80,128)
0.5787	0.5786	0.02%	5	531133	(108,172)
0.6887	0.6884	0.05%	15	622044	(152,244)
0.7052	0.7054	0.03%	5	622244	(160,256)
0.8078	0.8071	0.08%	30	604064	(208,336)

**Fig. 2.** (A and B) BSE images of two thin polished slices of the khatyrkite sample shown in Fig. 1. At least one microprobe analysis was made at each location marked with a symbol, corresponding to the following phases: khatyrkite ( $\text{CuAl}_2$ ), yellow squares; cupalite ( $\text{CuAl}$ ), blue circles; unknown mineral ( $\text{AlCuFe}$ ), corresponding to  $\beta$  phase (5, 12) in the synthetic alloy, purple triangles; forsteritic olivine [ $(\text{Mg}_{0.95}\text{Fe}_{0.05})_2\text{SiO}_4$ ], intimately associated with khatyrkite, green diamonds; and natural quasicrystal with approximate composition  $\text{Al}_{63}\text{Cu}_{24}\text{Fe}_{13}$ , red pentagons.



that all the phases were formed naturally by geologic processes and are unlikely to have been introduced by human activity; however, elucidating the mechanisms responsible for this heterogeneous morphology and for the low oxygen fugacity implied by the existence of metallic Al remains a serious and fascinating challenge. In addition to these phases, we observed within the sample a grain about 90 to 120  $\mu\text{m}$  across that, based on 18 microprobe analyses, is approximately  $\text{Al}_{65}\text{Cu}_{20}\text{Fe}_{15}$ , with an uncertainty of less than 0.1 atomic %. This is close to the optimal stoichiometry of synthetic i-AlCuFe (5). Over 200 microprobe samplings show that the chemical composition in each of the metallic phases shown in Fig. 2 has a fairly uniform composition. Extensive studies of AlCuFe alloy formation in the laboratory do not show the same assemblage of metal alloys found in this sample (13).

To investigate the atomic structure of this possible i-AlCuFe phase, we removed grains from the polished thin sections, mounted them on glass fibers, and collected powder XRD patterns with a diffractometer (14). The powder XRD pattern gives direct information about the atomic structure that can indicate whether it is a quasicrystal, using the scheme in (7). For an icosahedral quasicrystal, the diffraction scattering intensity in Fourier space at scattering vector  $\mathbf{q}$  is  $I(\mathbf{q}) = \sum |\rho_{\mathbf{Q}}|^2 \delta_{\mathbf{q}, \mathbf{Q}}$ , where  $\rho_{\mathbf{Q}}$  is complex, and the sum is over a discrete lattice of reciprocal vectors  $\mathbf{G}$ , expressible as integer linear combinations of the six fundamental wave vectors  $\mathbf{g}_k = [\sin \beta \cos(\frac{2\pi k}{5}), \sin \beta \sin(\frac{2\pi k}{5}), \cos \beta]$  for  $k = 0, \dots, 4$  and  $\cos \beta = \frac{1}{\sqrt{5}}$  and  $\mathbf{g}_5 = (0, 0, 1)$ . The vectors  $\{\mathbf{g}_k, \mathbf{g}_5\}$  are oriented along the six fivefold symmetry axes of an icosahedron (15). The icosahedron (which has the symmetry of a soccer ball) also has 10 threefold symmetry axes and 15 twofold symmetry axes. Associated with each peak  $\mathbf{Q}$  is a complementary wave vector  $\bar{\mathbf{Q}}$ , obtained by using the same six integers to construct the corresponding linear combinations of  $\bar{\mathbf{g}}_k = \mathbf{g}_{2k \bmod 5}$  and  $\bar{\mathbf{g}}_5 = -\mathbf{g}_5$ . The diffraction scattering intensity at peak  $\mathbf{Q}$  tends to decrease as  $|\bar{\mathbf{Q}}|$  increases. Synthetic i-AlCuFe is a face-centered icosahedral (FCI) quasicrystal (5); in these structures, Bragg peaks occur only at integer linear combinations of  $\{\mathbf{g}_k, \mathbf{g}_5\}$  where the sum of the integers is even. Applying the automated indexing program in (7), we compared the powder XRD pattern of our AlCuFe mineral grains to that of an ideal FCI structure and found that all of the major peaks (Fig. 3A) match closely with Bragg reflections in the ideal structure, as shown in Table 1. We also quantified the degree of conformity, using figures of merit corresponding to  $\bar{\Delta}$ , the intensity-weighted average of the absolute deviation of each  $\mathbf{Q}$  from its closest-matching FCI peak (column three in Table 1), and the intensity-weighted average of  $|\bar{\mathbf{Q}}|$ , as discussed in (7); Fig. 3B shows that the sample ranked extremely high.

To explore the atomic structure, several granules, each a few micrometers across (such as the one shown in Fig. 1B), were removed from the glass fiber and examined with TEM (16). On the submicrometer length scale, the grains are mostly homogeneous but contain some smaller domains with slightly different compositions. Some of these regions were found with energy-dispersive x-ray analysis to be  $\text{Al}_{63 \pm 1}\text{Cu}_{24 \pm 1}\text{Fe}_{13 \pm 1}$ , within an error equal to the known composition of synthetic i-AlCuFe. (This suggests that the electron microprobe analysis, which averages over larger domains, included regions with different compositions.) The diffraction patterns from these regions, obtained by tilting the sample at various angles, are shown in Fig. 4. These patterns, consisting of sharp peaks arranged in an

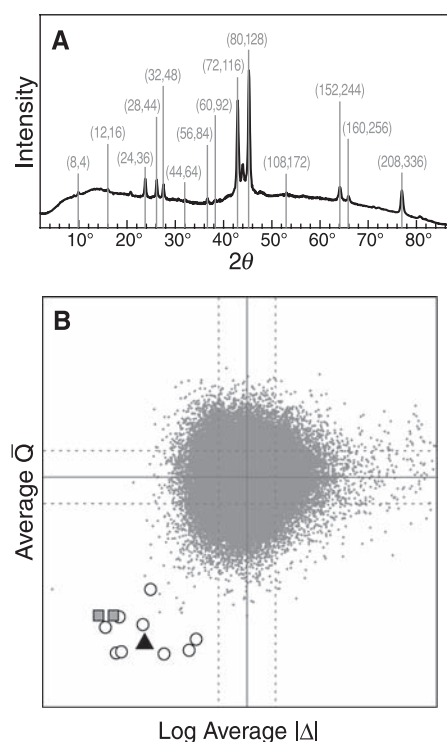


**Fig. 3. (A)** Powder XRD pattern for the natural sample, with major peaks indexed by the automated scheme in (7). The narrow sharp peaks indicate a high degree of translational order. **(B)** The distribution of two figures of merit introduced in (7) to separate quasicrystals from among a large collection of powder patterns in the ICDD-PDF: (i) the logarithm of the intensity-weighted average  $|\Delta|$ , where  $\Delta$  is the absolute deviation of each  $\bar{Q}$  from the closest-matching FCI peak (column three in Table 1); and (ii) the intensity-weighted average of  $\bar{Q}$ . Known synthetic FCI quasicrystals are indicated with gray squares (AlCuFe) and white circles (other examples). They cluster far from ordinary crystalline minerals (gray dots), whose average and standard deviation are indicated by solid and dashed lines, respectively. The natural sample, marked with the black triangle, is several standard deviations away from the average and well within the cluster of known FCI quasicrystals.

incommensurate lattice with five-, three-, and twofold symmetry, are the characteristic signature of an icosahedral quasicrystal (1, 5). In addition, the angles between the symmetry planes shown in Fig. 4 are consistent with icosahedral symmetry. For example, the angle between the two- and fivefold symmetry planes was measured to be  $31.6^\circ \pm 0.5^\circ$ , which agrees with the ideal rotation angle between the twofold and fivefold axes of an icosahedron ( $\arctan \frac{1}{\sqrt{5}} \approx 31.7^\circ$ ). The inverted Fourier transform of the high-resolution TEM (HRTEM) image shown in Fig. 1C shows that the real space structure consists of a homogeneous, quasiperiodic, and fivefold symmetric pattern. Together, these TEM results provide conclusive evidence of crystallographically forbidden icosahedral symmetry in a naturally occurring phase.

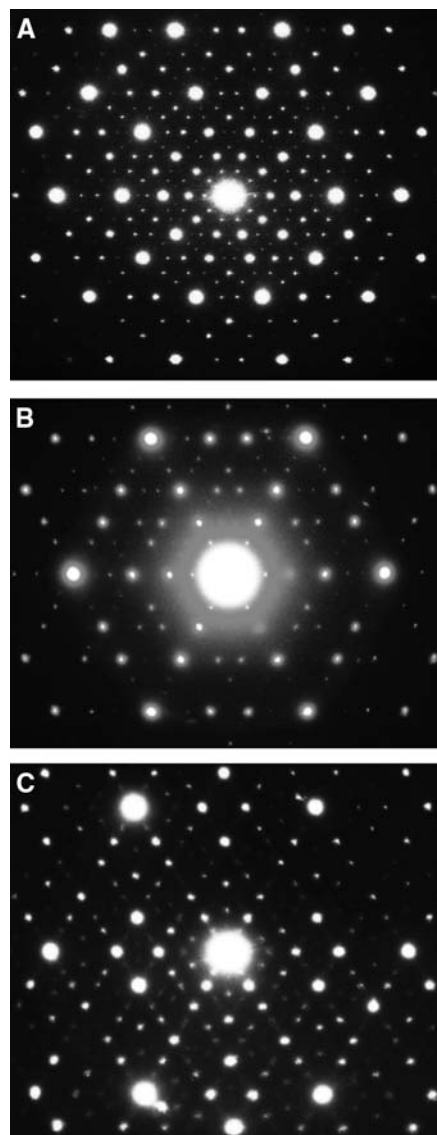


**Fig. 4.** The fivefold **(A)**, threefold **(B)**, and twofold **(C)** diffraction patterns obtained from a region (red dashed circle) of the granule in Fig. 1B match those predicted for a FCI quasicrystal, as do the angles that separate the symmetry axes.

TEM and XRD also demonstrated the high degree of structural perfection in the mineral quasicrystal. In the electron diffraction patterns in Fig. 4, there is no visible distortion. Quasicrystals produced by rapid quenching or embedded in a matrix of another phase often exhibit measurable deviations from the ideal pattern due to phason strains (15, 17). An experimental signature is a shift in Bragg peak positions relative to the ideal by an amount proportional to  $\bar{Q}$ , corresponding to larger shifts for peaks with smaller intensity. If the diffraction pattern is held at a grazing angle and viewed down rows of peaks, the phason strain can be observed as deviations of the dimmer peaks from straight rows (15). The diffraction patterns in Fig. 4 display no discernible evidence of phason strain. This qualitative observation is quantified by the XRD data in column three of Table 1, which demonstrate that the natural quasicrystal has a degree of structural perfection comparable to that of the best laboratory specimens (Fig. 3B). Either the mineral samples formed without phason strain in the first place, or subsequent annealing was sufficient for phason strains to relax away.

A nearly structurally perfect natural quasicrystal that formed under geologic conditions would have several implications for geology and condensed-matter physics. The definition of a mineral, which previously included periodic crystals, incommensurate structures (18, 19), and amorphous phases, would henceforth include quasicrystals, expanding the catalog of structures formed by nature and raising an interesting challenge to explain how they formed naturally. Finally, the study of natural quasicrystals may provide insights about the formation and stability of quasicrystals at temperatures and pressures not studied in the laboratory previously, and perhaps an avenue for discovering new quasicrystals with compositions not yet synthesized.

#### References and Notes

1. D. Levine, P. J. Steinhardt, *Phys. Rev. Lett.* **53**, 2477 (1984).
2. D. Shechtman, I. Blech, D. Gratias, J. W. Cahn, *Phys. Rev. Lett.* **53**, 1951 (1984).
3. R. Penrose, *Bull. Inst. Math. Appl.* **10**, 266 (1974).
4. C. Janot, *Quasicrystals: A Primer* (Oxford Univ. Press, Oxford, 1994).
5. P. A. Bancel, *Quasicrystals: The State of the Art*, D. DiVincenzo, P. J. Steinhardt, Eds. (World Scientific, Singapore, 1991), pp. 17–56.
6. A. P. Tsai, A. Inoue, T. Masumoto, *Jpn. J. Appl. Phys.* **26**, L1505 (1987).
7. P. J. Lu, K. Deffeyes, P. J. Steinhardt, N. Yao, *Phys. Rev. Lett.* **87**, 275507 (2001).
8. L. V. Razin, N. S. Rudashevskij, L. N. Vyalsov, *Zapiski Vses. Mineralog. Obshch.* **114**, 90 (1985).
9. F. C. Hawthorne *et al.*, *Am. Mineral.* **71**, 1277 (1986).
10. N. I. Filatova, V. S. Vishnevskaya, *Tectonophysics* **269**, 131 (1997).
11. The instrument was a Zeiss-EVO MA15 scanning electron microscope coupled with an Oxford INCA250 energy-dispersive spectrometer, operated with 25-kV accelerating voltage, 500-pA probe current, 2500 counts per second as average count rate on the whole spectrum, and counting time of 100 s. Samples were sputtered with 30-nm-thick carbon film.
12. The instrument was a JEOL JXA-8600 electron microprobe, using a 20-kV accelerating voltage; 40-nA

- beam current; 30-s counting time; and Al-K $\alpha$ , Cu-K $\alpha$ , and Fe-K $\alpha$  lines.
13. L. Zhang, R. Lüch, Z. Metallkd. **94**, 774 (2003).
  14. The instrument was an Oxford Diffraction Excalibur PX Ultra diffractometer with a 165-mm diagonal Onyx charge-coupled device detector at 2.5:1 demagnification. The program *Crysalis RED* (Oxford Diffraction 2006) was used to convert the observed diffraction rings into a conventional XRD pattern.
  15. T. C. Lubensky, J. E. S. Socolar, P. J. Steinhardt, P. A. Bancel, P. A. Heiney, *Phys. Rev. Lett.* **57**, 1440 (1986).
  16. The instrument was a Philips CM200-FEG TEM configured with a super-twin lens. The instrument was operated at 200 kV with a vacuum pressure of  $\sim 2 \times 10^{-7}$  torr; the electron beam size ranged from 50 nm to 0.3  $\mu\text{m}$ .
  17. D. Levine, T. C. Lubensky, S. Ostlund, S. Ramaswamy, P. J. Steinhardt, J. Toner, *Phys. Rev. Lett.* **54**, 1520 (1985).
  18. B. Dam, A. Janner, J. D. H. Donnay, *Phys. Rev. Lett.* **55**, 2301 (1985).
  19. E. Makovicky, B. G. Hyde, *Struct. Bonding* **46**, 101 (1981).
  20. We are indebted to L. Hollister and G. MacPherson for their critical examination of the results, especially regarding the issue of natural origin. We also thank P. Bonazzi, K. Deffeyes, S. Menchetti, and P. Spry for useful discussions and S. Bambi at the Museo di Storia Naturale for the photograph of the original sample in

Fig. 1A. L.B. thanks the Ministero dell'Istruzione dell'Università e della Ricerca Programma di Ricerca Nazionale 2007 project "Complexity in minerals: modulation, phase transition, structural disorder," issued to S. Menchetti. This work was supported in part by U.S. Department of Energy grant DE-FG02-91ER40671 (P.J.S.), the NSF MRSEC program through New York University (grant DMR-0820341; P.J.S.), the Princeton Center for Complex Materials (grant DMR-0819860; N.Y.), and the New Jersey Commission of Science and Technology (N.Y.).

12 January 2009; accepted 23 March 2009  
10.1126/science.1170827

# Observation of Single Colloidal Platinum Nanocrystal Growth Trajectories

Haimei Zheng,<sup>1,2,3</sup> Rachel K. Smith,<sup>3\*</sup> Young-wook Jun,<sup>2,3\*</sup> Christian Kisielowski,<sup>1,2</sup> Ulrich Dahmen,<sup>1,2†</sup> A. Paul Alivisatos<sup>2,3†</sup>

Understanding of colloidal nanocrystal growth mechanisms is essential for the syntheses of nanocrystals with desired physical properties. The classical model for the growth of monodisperse nanocrystals assumes a discrete nucleation stage followed by growth via monomer attachment, but has overlooked particle-particle interactions. Recent studies have suggested that interactions between particles play an important role. Using in situ transmission electron microscopy, we show that platinum nanocrystals can grow either by monomer attachment from solution or by particle coalescence. Through the combination of these two processes, an initially broad size distribution can spontaneously narrow into a nearly monodisperse distribution. We suggest that colloidal nanocrystals take different pathways of growth based on their size- and morphology-dependent internal energies.

The growth of colloidal nanocrystals has advanced remarkably, and now it is possible to make colloidal nanocrystals of a wide range of solids, ranging from metals to semiconductors and insulators, with narrow size distributions (variations in diameter less than 5%) and high crystallinity (1–5). It is also possible to control their shapes, from spheres to disks or rods, as well as their topology (solid, hollow, nested) and their connectivity and branching patterns by adjusting the growth parameters, such as surfactant, concentration, or temperature (6–11). The current state of nanocrystal synthesis has been largely achieved empirically with some classical models (12–14) for particle growth serving as guides. Here, we demonstrate that it is possible to directly observe the growth trajectories of individual colloidal nanocrystals in solution by using a liquid cell that operates inside a transmission electron microscope (TEM), and that these trajectories reveal a set of pathways more complex than those previously envisioned.

Consider the simplest case of a narrow size distribution of nearly spherical colloidal nanoparticles. A model based on kinetics that can account for this size distribution was proposed by LaMer and Dinegar (12) and improved by Reiss (13). An abrupt increase in monomer concentration induces a burst of nucleation events followed by a period of rapid growth. The initial broad size distribution because of a spread in nucleation time

or other variations such as mixing can be corrected with "size distribution focusing," in which small crystals "catch up" with larger ones because the growth rate of nanocrystals decreases as the size increases (1). Inhibition of particle aggregation is typically achieved by using surfactant ligands that stabilize the particle surface and provide a barrier to coalescence. The thinking underlying this approach has guided many syntheses (1, 2, 4). A second scenario for nanocrystal control employs an equilibrium approach. One devises a system in which the binding of surfactant to the nanoparticle surface is nearly as strong as the bonds within the crystal, strong enough then to thermodynamically drive the system toward a particular average size for a given concentration of surfactant and monomeric species (15–17). These two distinct models consider only the possibility of particle growth through the addition of monomeric species. However, there is substantial evidence that particle coalescence or even oriented attachment can also play a role in nanocrystal growth (18–22). The lack of consensus on the controlling mechanisms is mainly due to the lack of direct evidence for nanocrystal growth in solution. In situ observation of the dynamic growth process is expected to substantially advance our understanding of nanocrystal growth mechanisms,

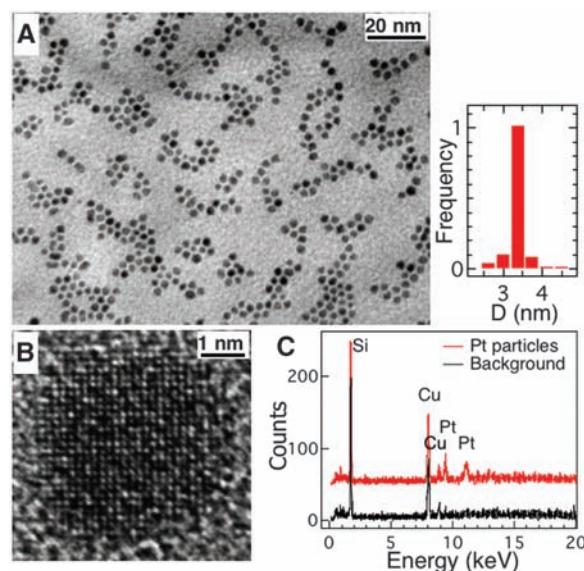


**Fig. 1.** TEM of Pt nanocrystals synthesized in a liquid cell. (A) Bright-field TEM image of Pt nanocrystals with a histogram of particle size distribution, obtained from measurements of 150 particles. (B) High-resolution TEM image of a Pt nanocrystal, which was recorded after the in situ experiment. (C) EDS spectra from Pt nanocrystals (red) and background (black) obtained ex situ from the same liquid cell. The observed Si and Cu signals are from the silicon nitride membrane window and the cover of the liquid cell, respectively.

<sup>1</sup>National Center for Electron Microcopy, Lawrence Berkeley National Laboratory, Berkeley, CA 94720, USA. <sup>2</sup>Materials Sciences Division, Lawrence Berkeley National Laboratory, Berkeley, CA 94720, USA. <sup>3</sup>Department of Chemistry, University of California, Berkeley, CA 94720, USA.

\*These authors contributed equally to this paper.

†To whom correspondence should be addressed. E-mail: udahmen@lbl.gov (U.D.); alivis@berkeley.edu (A.P.A.)